BJR

Received: 23 December 2016 | Revised: 25 May 2017 | Accepted: 6 June 2017

https://doi.org/10.1259/bjr.20170007

Cite this article as:
Jerjir N, Bruyneel L, Haspeslagh M, Quenet S, Coenegrachts K. Intravoxel incoherent motion and dynamic contrast-enhanced MRI for differentiation between hepatocellular adenoma and focal nodular hyperplasia. *Br J Radiol* 2017; **90**: 20170007.

FULL PAPER

Intravoxel incoherent motion and dynamic contrast-enhanced MRI for differentiation between hepatocellular adenoma and focal nodular hyperplasia

[1]NAIM JERJIR, MD, [2]LUK BRUYNEEL, PhD, [3]MARC HASPESLAGH, PhD, [4]SARAH QUENET, BEng and [1]KENNETH COENEGRACHTS, MD, PhD

[1]Department of Radiology, AZ St.-Jan Brugge-Oostende AV, Bruges, Belgium
[2]Institute for Healthcare Policy, KU Leuven—University of Leuven, Leuven, Belgium
[3]Hospital Administration and Statistics, AZ St.-Jan Brugge-Oostende AV, Bruges, Belgium
[4]Olea Medical, La Ciotat, France

Address correspondence to: Prof. Dr. Kenneth Coenegrachts
E-mail: *kenneth.coenegrachts@azsintjan.be*

Objective: To examine if intravoxel incoherent motion (IVIM) and dynamic contrast-enhanced MRI (DCE-MRI) can be used as new and supplemental MRI techniques to differentiate hepatocellular adenomas (HCAs) from focal nodular hyperplasias (FNHs) and analyse if diffusion parameter apparent diffusion coefficient (ADC) and IVIM parameter true diffusion coefficient (D) differ in doing so.

Methods: This prospective study included 21 patients (8 HCAs and 13 FNHs) who underwent a specifically designed MRI scanning protocol, including series for analysis of IVIM (four *b*-values 0, 10, 150 and 800 s mm^{-2}) and DCE-MRI. On a dedicated workstation, identical regions of interest were placed in parametric maps of K^{trans}, V_e, D and ADC in each lesion for quantification. Diagnostic accuracy was assessed using receiver operating characteristics analysis. Time–intensity curves (TICs) were classified in different types.

Results: HCAs had significantly lower values for K^{trans} (mean 1.45 *vs* 2.68 min^{-1}; $p = 0.029$) and D (mean 1.02×10^{-3} *vs* 1.22×10^{-3} mm^2 s^{-1}; $p = 0.033$). Both parameters showed good diagnostic accuracy of 76%. TIC analysis could not differentiate between HCAs and FNHs.

Conclusion: In this exploratory study, K^{trans} and D were able to differentiate HCAs from FNHs in most cases, whereas V_e, ADC and TIC analysis were not.

Advances in knowledge: Histological differences between HCAs and FNHs can be quantified on MRI using K^{trans} and D.

INTRODUCTION

Diffusion-weighted MRI (DW-MRI) has become a routinely implemented radiological tool for the assessment of microscopic morphological features of tissues on a macroscopic level. More specifically, the diffusion pattern of water molecules *in vivo* is dependent on the architectural properties of the biological tissue, such as the tissue type or whether the tissue is pathological. However, DW-MRI is not only sensitive for true molecular diffusion but also for other "incoherent motions".[1] The orientation of the capillary network is nearly random, which is why blood flow will mimic the random motion of water molecules and contaminate the signal from the real molecular diffusion in diffusion weighted (DW) images ("pseudodiffusion").[1,2] Interestingly, the pseudodiffusion coefficient is roughly ten-fold higher than the diffusion coefficient.[3] This explains why the signal of pseudodiffusion will only contribute to DW-MRI images when low *b*-values are applied.[1–5] In contrast to the apparent diffusion coefficient (ADC), "true diffusion" (D) does not take the contamination of the incoherent motions into account and is only dependent on diffusion restriction measured with high *b*-values.

The most commonly used application of dynamic contrast-enhanced MRI (DCE-MRI) consists of intravascular injection of a gadolinium-based contrast agent, after which multiple (dynamic) T_1 weighted (T1w) images are acquired. Within a voxel, or more commonly a region of interest (ROI), the changes in relative intensity are monitored over time. Plotting of this data allows for semi-quantitative analysis in the form of a time–intensity curve (TIC).[6,7] When a tracer-kinetic model is used to represent the different tissue compartments (intravascular space and extravascular extracellular space), quantitative analysis of the DCE-MRI data can be obtained to characterize the

microcirculation of the tissue.[6–9] The most essential quantitative parameters are K^{trans} (transfer constant), which reflects the transport of contrast across the vessel wall into the extravascular extracellular space ("permeability"), and V_e (the fraction of extracellular extravascular volume), reflecting the cellular density.

Differentiation between hepatocellular adenoma (HCA) and focal nodular hyperplasia (FNH) is important and might influence outcome, therapeutic consequences and follow-up strategies. Unlike FNH, HCA carries the risk of malignant transformation and bleeding, especially in larger lesions and with specific histological subtypes.[10–12] Our purpose was to examine if intravoxel incoherent motion (IVIM) and DCE-MRI can be used as new and supplemental MRI techniques to differentiate HCAs from FNHs and to examine if ADC and *D* differ in doing so.

METHODS AND MATERIALS

Patients

In this prospective study, 38 consecutive patients with focal liver lesions underwent liver gadolinium-enhanced MRI (Gd-BOPTA; MultiHance®, Bracco, Italy) with a specifically designed scanning protocol between November 2013 and February 2015, after which they were assigned to a separate database in our picture archiving and communication system (PACS—IMPAX; Agfa, Mortsel, Belgium). The review board of our institution (AZ St.-Jan Brugge-Oostende AV). Only patients with a lesion of at least 2 cm were included. Only one lesion per patient was analysed. 17 patients were excluded from the study [focal liver lesion different than HCA or FNH ($n = 10$); lesion <2 cm ($n = 4$); no focal lesion found ($n = 2$); and incomplete scanning protocol ($n = 1$)]. 21 patients were included in the study, 8 with HCA (all 8 females) and 13 with FNH (11 females and 2 males). Differentiation between FNH and HCA was based on different criteria: pathological verification ($n = 1$), typical morphological properties [arterially hyperenhancing, showing no washout in the venous phase, the absence of cirrhosis, typical central scar, lesion heterogeneity and the presence of fat/signal decrease on out-of-phase imaging ($n = 20$)] and behaviour of the lesions in follow-up [clear decrease in dimension after stop of oral contraceptive medication ($n = 6$), increase in dimension at follow-up ($n = 1$)]. A detailed list of the behaviour of the lesions in follow-up studies is shown in Table 1. The most

Table 1. Behaviour of the lesions in follow-up studies

Lesion	Behaviour of the lesion	Time since study MRI
HCAs		
Lesion 1	Decrease in volume	11 months
Lesion 2	Decrease in volume	12 and 24 months
Lesion 3	No follow-up at our institution	/
Lesion 4	Decrease in volume	14 months
Lesion 5	Decrease in volume	12 months
Lesion 6	Decrease in volume	4 and 16 months
Lesion 7	Decrease in volume	4, 9 and 21 months
Lesion 8	Increase in volume; follow-up at a different institution[a]	12 months
FNHs		
Lesion 1	Stable	12 and 24 months
Lesion 2	Stable	28 months
Lesion 3	Stable	24 months
Lesion 4	Stable	22 months
Lesion 5	No follow-up at our institution	/
Lesion 6	Stable	6, 12 and 18 months
Lesion 7	Stable	14 and 19 months
Lesion 8	No follow-up at our institution	/
Lesion 9	No follow-up at our institution	/
Lesion 10	No follow-up at our institution	/
Lesion 11	Stable	9 months
Lesion 12	Stable	22 and 37 months
Lesion 13	No follow-up at our institution	/

FNH, focal nodular hyperplasia; HCA, hepatocellular adenoma.
[a]The authors contacted the different institution to analyse and compare the MRI images.

important differential diagnosis is hepatocellular carcinoma (HCC). None of the included lesions showed signs of HCC (such as washout in the venous phase nor cirrhotic liver background). Moreover, in contrast to HCA, HCC is not to be expected to show a volume decrease in follow-up studies, as six out of eight HCAs did after only stopping intake of oral contraceptive medication.

Imaging technique

All patients underwent an MRI examination with a 3-T superconductive MR system (Philips Ingenia 3T release 4, Best, Netherlands) and a 32-channel body phased-array coil. The MRI protocol consisted of axial breath-hold (BH) dual fast field echo, axial respiratory-triggered single shot (SS) spin-echo echo planar imaging (SE-EPI) with single low *b*-value ($10\,s\,mm^{-2}$), axial respiratory-triggered SS SE-EPI using four *b*-values (0, 10, 150 and $800\,s\,mm^{-2}$), followed by an axial BH T1w gradient echo (DCE-MRI) sequence.

We limited the SS SE-EPI (DW) sequence to four *b*-values, as more *b*-values would mean an increase in scanning time, making it impractical for clinical use. Parameters consisted of: matrix: 350×325 mm; measured voxel size: $2.3 \times 2.7 \times 5$ mm; parallel imaging (AP): 2.4; repetition time: 1200 ms; echo time: 78 ms; echo planar imaging factor: 49; fat suppression using selective partial inversion recovery; number of signal averages: 2.

The DCE-MRI sequence was performed using a BH T1w gradient echo sequence with keyhole imaging and profile sharing after injection of $0.1\,ml\,kg^{-1}$ body weight gadobenate dimeglumine followed by a 20-ml saline injection at $3\,ml\,s^{-1}$. Imaging was started when initial contrast enhancement of the right ventricle occurred during fluoroscopic imaging. A total of 1995 images (15 sets of whole liver imaging sets comprising 133 images each) were acquired per patient, with the following schedule:

(1) 5 sets of images during the first BH of 13.8 s; a break of 7 s to allow for breathing and without image acquisition
(2) 4 sets of images during the second BH of 12.6 s; a break of 7 s
(3) 3 sets of images during the third BH of 11.4 s; a break of 7 s
(4) 2 sets of images during the fourth BH of 10.2 s; a break of 7 s
(5) 1 set of images during the fifth (last) BH of 9 s.

Some additional parameters of the T1w DCE-MRI sequence consisted of: matrix: 395×295 mm; measured voxel size: $1.4 \times 1.7 \times 3$ mm; parallel imaging (anteroposterior AP): 2 and (feet-head FH): 1.8; turbo field echo factor: 56; flip angle: 10°; fat suppression using spectral attenuated inversion recovery.

Image analysis—dynamic contrast-enhanced MRI and intravoxel incoherent motion

New software (OleaSphereTM; Olea Medical SA, La Ciotat, France) was used. With this software, a dedicated workflow was designed, which made it possible to analyse the DCE-MRI and IVIM data sequentially by following the same steps in every patient. One of the authors (NJ) with 4 years of experience in abdominal imaging performed the analysis. The data of all the patients were analysed after all the MRI examinations were performed. The patients' MRI examinations were loaded from the PACS into the dedicated workstation with the Olea software. After selecting a specific patient and activating the workflow, the first step was to select the type of function to describe the DW-MRI data, *i.e.* biexponential function in case of IVIM. Rigid registration was selected. In the next step, we optimized the DCE-MRI parameters using the T1w images after gadolinium injection to consistently place the region of the arterial input function in the descending aorta, approximately 5 cm above the origin of the celiac trunk to reduce turbulence artefacts.

The software allowed us to select the extended Tofts model as the tracer-kinetic model. Automatic motion correction for breathing is a feature of the software. Following those steps, we automatically obtained parametric maps of the entire liver of K^{trans} and V_e (the two forming "permeability maps") and *D*, as well as T_2 images of the entire liver for anatomical correlation (Figure 1). Other MRI sequences could be used as well but were not selected to ensure a clear overview. A ROI delineated in one of the parametric maps was automatically copied in the other parametric maps, which yielded detailed quantification of K^{trans}, V_e and *D* as well as a TIC. Values for D^* ("pseudodiffusion") and f ("perfusion fraction") were not analysed since these could not be confidently measured by the software when using only four *b*-values and because of the great interobserver variation and low reproducibility even when using more *b*-values.[13–15]

When a mismatch was noticed between the position of the ROI on the diffusion and permeability parametric maps, the ROI was manually adjusted to match the lesion. ROIs were drawn peripherally in the lesion so that they would enclose as much of the lesion as possible, with a 2-mm safety margin to the outer border of the lesion. Ultimately, screen shots and the quantitative data were saved to the PACS and hard drive, respectively, and the TICs were categorized.

For analysis of the ADC, a separate workflow was chosen after selecting the patient. Just as in the first step of the previous workflow, the type of function to describe the DW-MRI data was chosen, *i.e.* the monoexponential function. In the next and final step, this resulted in an ADC map. The ROI from the previous workflow was manually copied in the ADC map, resulting in quantification of the ADC.

Statistical analysis

Firstly, independent sample *t*-tests were used to determine whether the mean scores of the variables under study (K^{trans}, V_e, *D* and ADC) for HCAs differed significantly from the mean scores for FNHs.

Secondly, logistic regression analyses were conducted to identify scores that discriminate between HCAs (coded "1") and FNHs (coded "0"). Sensitivity and specificity were calculated for receiver operating characteristic (ROC) curves. We tested the statistical significance of the difference between the areas under the ROC (AUROC) curves for our variables under study. Optimal cut-points were explored through the criterion value corresponding with the Youden[16] index J. J is the maximum vertical distance between the ROC curve and the diagonal line, which gives equal weight to sensitivity and specificity. The ROC

Figure 1. Example of the layout in Olea (Olea Medical SA, La Ciotat, France) in the last step ("analysis") of the dedicated workflow in a patient with focal nodular hyperplasia (FNH). The layout is divided into six smaller screens (a–f). T_2 weighted images in the right upper corner are used for anatomical correlation and show the lesion within the right liver lobe (b). The parametric maps of apparent diffusion coefficient and "true diffusion" D reflect the degree of diffusion restriction, ranging from dark areas of restricted diffusion to white areas of nearly free diffusion (c, d). Colour parametric maps of K^{trans} and V_e can be adjusted so that they easily display the lesion (e, f). After drawing a ROI (on a different slice, not shown) in the lesion in one of the parametric maps, a time–intensity curve appears in the left upper corner (a). This FNH showed to have a Type 1 curve.

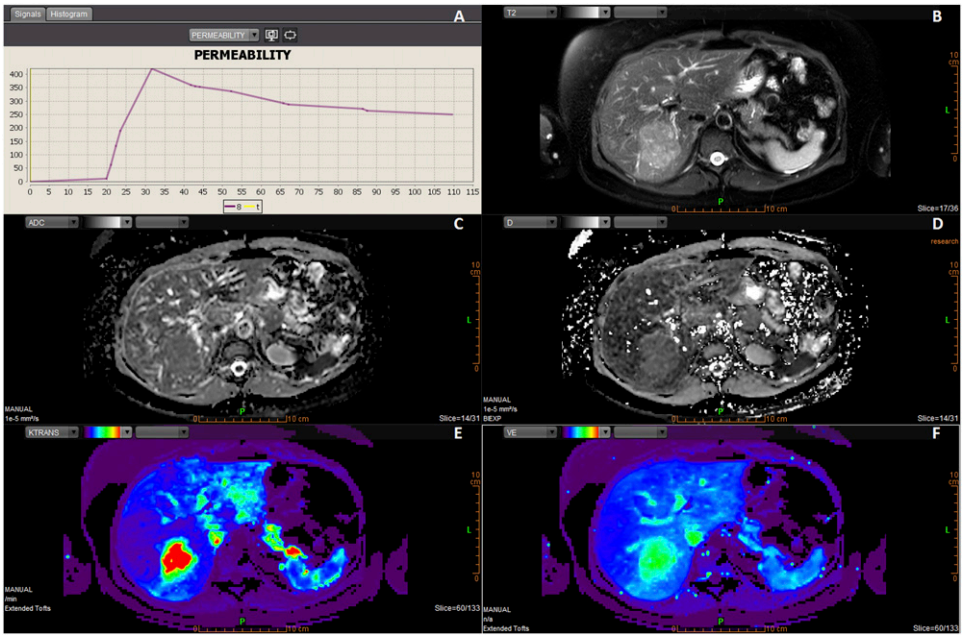

curve and classification table were further examined as, from a clinical perspective, we prioritized a high sensitivity of the variables for detecting HCAs in order to ensure proper follow-up of or the right treatment for these lesions. As such, our clinical interpretation of the optimal cut-point did not necessarily correspond to the Youden index J-associated criterion. The data analysis for this article was generated using SAS software v. 9.4 (SAS Institute Inc., Cary, NC) for Windows®.

Thirdly, based on the cut-points, the variables under study were dichotomized, and the sensitivity and specificity were again assessed in a model that combined these possible predictors.

RESULTS

Evaluation of the time–intensity curves

According to the literature,[17] TICs can be classified into two types. Type 1 has a steep enhancement followed by a quick decay and then a slowly decaying plateau (Figure 2a). Type 2 curves have a steep enhancement followed by a slowly decaying plateau (Figure 2b). 6 out of 8 HCAs (75%) and 10 out of 13 FNHs (77%) had a Type 1 curve. One HCA (13%) and one FNH (8%) were characterized by a Type 2 curve. One HCA (13%) and two FNHs (15%) could not be categorized into a Type 1 or Type 2 curve, with all three lesions being located in the left liver lobe.

Evaluation of the quantitative data

Table 2 shows that HCAs had lower values for all parameters than FNHs. Statistically significant differences between K^{trans} (mean 1.45 *vs* 2.68 min^{-1}; $p = 0.029$) and D (mean 1.02×10^{-3} *vs* 1.22×10^{-3} $mm^2 s^{-1}$; $p = 0.033$) were found. There were no statistically significant differences for V_e (mean 0.35 *vs* 0.43; $p = 0.189$) or ADC (mean 1.41×10^{-3} *vs* 1.57×10^{-3} $mm^2 s^{-1}$; $p = 0.214$).

Sensitivity and specificity

The ability of K^{trans} and D to differentiate HCAs from FNHs was further explored by generating ROC curves. With an AUROC of 0.76 [95% confidence interval (CI): 0.53–0.92; $p = 0.023$] and 0.79 (95% CI: 0.56–0.93; $p = 0.008$), respectively, both K^{trans} and D demonstrated the ability to differentiate both lesion types. No statistically significant difference between the AUROCs of K^{trans} and D was found ($p = 0.872$). This indicates that both parameters perform equally well in differentiating HCAs from FNHs. For D, the optimal cut-point was $\leq 1.05 \times 10^{-3}$ $mm^2 s^{-1}$ with a sensitivity of 75% (6/8; 95% CI: 35–97) and a specificity of 77% (10/13; 95% CI: 46–95). For K^{trans}, the optimal cut-point was ≤ 1.40 min^{-1} with a sensitivity of 75% (6/8; 95% CI: 35–97) and specificity of 77% (10/13; 95% CI: 46–95). Accuracy (the percentage of correct diagnoses in the entire sample) equalled 76% for both cut-points. The combined cut-points for K^{trans} and D are associated with a sensitivity of 50%, a specificity of 100% and an accuracy of 52%.

DISCUSSION

Our study showed that IVIM parameter D and DCE-MRI parameter K^{trans} were both able to differentiate HCAs from FNHs, meaning that they could detect the histological differences between the two types of lesions. For both parameters, the values

Figure 2. Time–intensity curves. Time (in seconds) on the *x*-axis and relative signal intensity (SI; in arbitrary units) on the *y*-axis. (a) Type 1 curve in a patient with focal nodular hyperplasia (FNH). Most FNHs and hepatocellular adenomas (HCAs) show a Type 1 curve with steep enhancement followed by a quick decay and then a slowly decaying plateau. (b) Type 2 curve in a patient with HCA. This curve follows a steep enhancement followed by a slowly decaying plateau. A Type 2 curve could be observed in one patient with HCA and one patient with FNH.

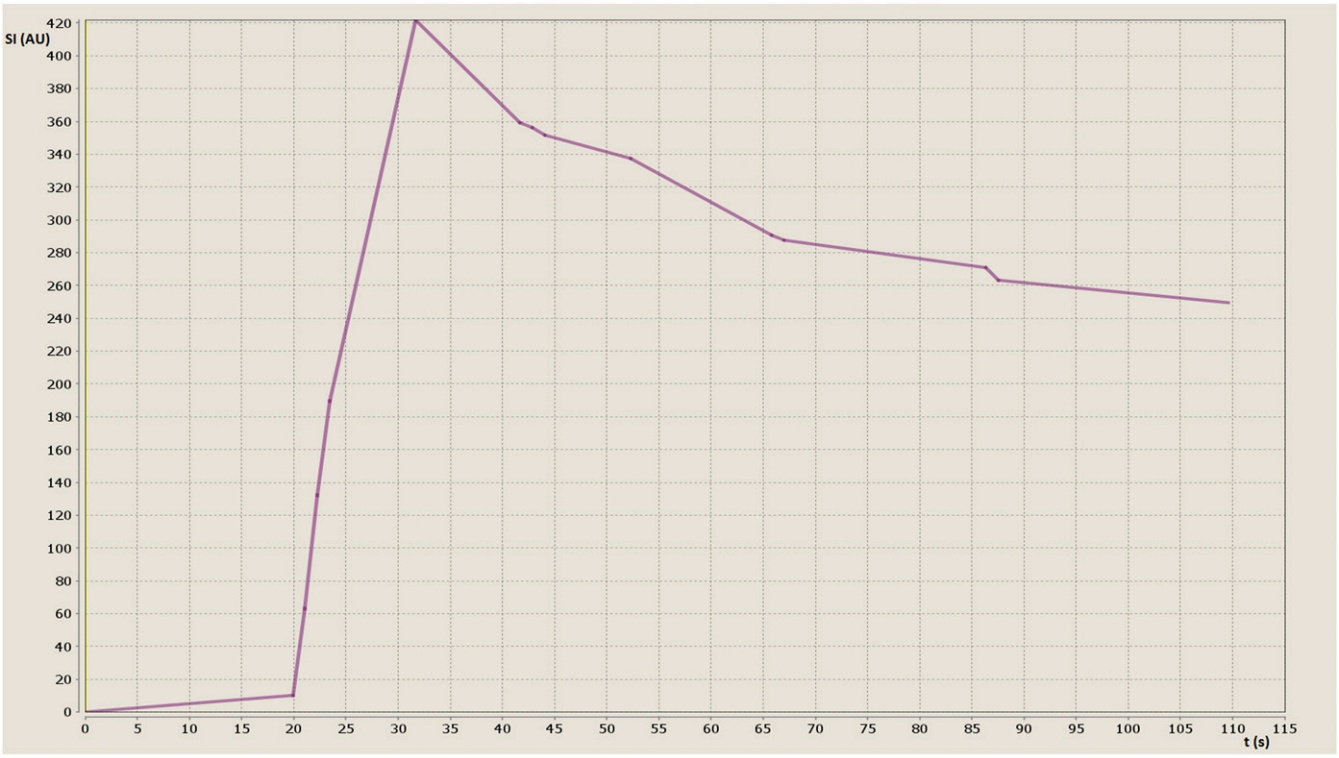

(a)

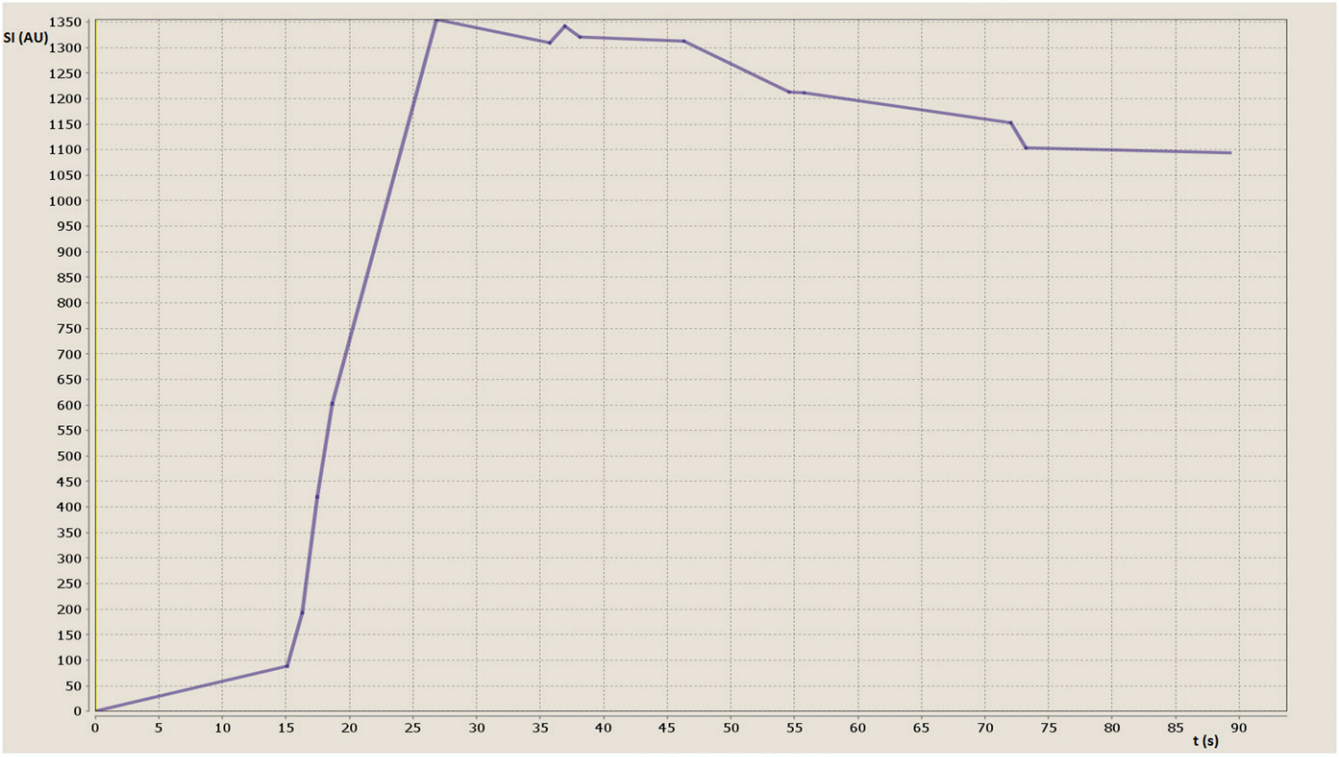

(b)

Table 2. Results of the transfer constant—K^{trans} (min^{-1}), the fraction of extracellular extravascular volume—V_e, true diffusion coefficient—D ($\times 10^{-3}$ mm s^{-1}) and apparent diffusion coefficient—ADC ($\times 10^{-3}$ mm s^{-2}) for focal nodular hyperplasias (FNHs) ($n = 13$) and hepatocellular adenomas (HCAs) ($n = 8$)

parameter	lesion	Mean	Standard deviation	Standard error of the mean	p-value
K^{trans}	FNH	2.68 (0.64–5.50)	1.36	0.38	0.029
	HCA	1.45 (0.86–2.99)	0.73	0.26	
V_e	FNH	0.43 (0.24–0.63)	0.13	0.04	0.189
	HCA	0.35 (0.15–0.47)	0.11	0.04	
D	FNH	1.22 (0.85–1.68)	0.22	0.06	0.033
	HCA	1.02 (0.93–1.25)	0.12	0.04	
ADC	FNH	1.57 (1.03–2.16)	0.28	0.08	0.214
	HCA	1.41 (0.93–1.81)	0.28	0.10	

were significantly lower in HCAs than in FNHs. The performance of D and K^{trans} to differentiate the two lesion types was identical: for D, a value of $\leq 1.05 \times 10^{-3}$ mm^2 s^{-1} indicated that the lesion was an HCA with a sensitivity of 75% and a specificity of 77%; a K^{trans} of ≤ 1.40 min^{-1} was indicative for an HCA with the same sensitivity and specificity, *i.e.* 75% and 77%, respectively. The ADC and IVIM parameter V_e were not able to differentiate between HCAs and FNHs.

TICs can be classified according to their enhancement pattern (Figure 2) into Type 1 and Type 2 curves. In our study, TIC characterization was not useful in differentiating the two lesion types. FNHs and HCAs both typically had a Type 1 curve, but one lesion in each group was characterized by a Type 2 curve. Furthermore, the TIC of one HCA and two FNHs did not show a pattern typical for a Type 1 or Type 2 curve and remained unclassified. These three unclassifiable lesions were located in the left liver lobe, suggestive of cardiac motion artefacts.

Morphological MRI features of both FNH and HCA have extensively been described in the literature.[10,11] Extracellular and, more recently, hepatocyte-specific gadolinium-based contrast agents have proved their value in differentiating focal liver lesions.[18–23] Grieser et al[18] showed that for differentiating HCAs from FNHs, the use of gadoxetic acid uptake in the hepatobiliary phase was superior to other morphological and dynamic vascular criteria. DW-MRI has also been used to differentiate the two lesion types. In a study with 54 FNHs and 36 HCAs, Agnello et al[24] found a significant difference between both lesions using ADC. However, it remained unclear what the influence of the perfusion-related incoherent motions was on the overall ADC values because no IVIM analysis was performed.

Our study now suggests that there is indeed a difference in true tissue diffusion between FNHs and HCAs, based on fundamental histological differences between these two types of lesions.[10,11] Few other studies analysed D and/or ADC values of multiple benign and malignant liver lesions but could not find a significant difference between FNHs and HCAs.[25,26] In our study, we did find a significant difference for D but not for ADC. Discrepancies in reports of D and ADC in their ability to characterize liver lesions are well known. In some studies, D was found to be superior to ADC in differentiating malignant from benign liver lesions,[27,28] whereas other studies showed the opposite.[29,30] These differences could be explained by different technical parameters, including the low number of included lesions in some studies and—when differentiating between malignant and benign lesions—by different types of included lesions.

For the "exact" calculation of IVIM parameters, it is best to use multiple low b-values as there is exponential (non-linear) signal decay in the low b-value range. In clinical practice, the use of multiple (*e.g.* 10) b-values is impractical because of long scanning times, which also potentially induces patient movements. For clinical purposes, in this study only four b-values were used. It has been proved that 4 b-values instead of 11 or even 16 b-values can be applied without affecting the precision of the IVIM parameters and test–retest reproducibility while reducing 75% or even more of the scanning time. Two optimized b-value distributions with only four b-values have recently been proposed. Dyvorne et al[13] suggested 0, 15, 150 and 800 s mm^{-2} as an optimal set, whereas Leporq et al[31] proposed 0, 10, 80 and 800 s mm^{-2}. In our study, we did not analyse IVIM parameters D^* and f because of the known intermediate-to-poor parameter reproducibility.[13–15] Future technical advances such as new hardware might overcome these limitations.

In one study with 52 FNHs, DCE-MRI with TIC analysis showed a Type 1 curve (fast enhancement and fast decay after reaching a peak) in all lesions.[17] Our study now suggests that not all FNHs show a fast decay but that it is possible for an FNH to reach a short plateau after the fast enhancement. To our knowledge, TIC analysis has not been performed up until the hepatobiliary phase. Grazioli et al[32] showed that with Gd-BOPTA, 100% of HCAs were hypointense in the hepatobiliary phase on T1w sequences, whereas 96.9% of the FNHs were hyper- or isointense. An expected course of the TIC after the decay would be a plateau for the FNHs and a continued decrease until the initial level for HCAs, which is the opposite of what happens in the arterial and portal venous phases.

To our knowledge, only one study has tried to differentiate FNHs from HCAs using DCE-MRI. The authors used a quantitative method, in which a significantly higher contrast ratio of FNHs was found than HCAs in the hepatobiliary phase after 15 and 25 min.[26] However, the long scanning time makes it less practical for clinical use. Our semi-quantitative analysis of the TICs reflecting the first pass of the contrast agent can be performed much faster (DCE-MRI scan time of 85 s after injection of contrast agent) but did not show a difference between both lesion types in our study.

Conversely, no study has previously examined the permeability parameters when differentiating FNHs from HCAs. Our study shows that there is a difference in K^{trans} between both lesions, with a higher permeability in FNHs, *i.e.* a higher amount of gadolinium molecules reaching the extravascular compartment through the endothelium in FNHs compared with HCAs.

HCAs and FNHs are vastly different lesions. HCA is a heterogeneous group of neoplasms consisting of inflammatory adenomas (with intense polymorphous inflammatory infiltrates on histopathology), hepatocyte nuclear factor 1α-muted adenomas (leading to hepatocellular proliferation and intracellular fat deposition) and β-catenin-mutated adenomas (which have a high nuclear cytoplasmic ratio).[10] On the other hand, both classic and non-classic FNHs are regenerative lesions. The classic type represents 80% of these lesions and consists of nodular hyperplastic liver tissue nodules surrounded by radiating fibrous septa originating from a central scar.[11] These histological differences might explain the higher diffusion restriction and thus lower D values in HCAs. The higher K^{trans} values in FNHs might be explained by a higher arterial inflow (when compared with HCAs) as the fibrous septa within FNHs contain the portal triad of an artery, vein and bile duct. As a consequence, the higher arterial influx is likely to represent a higher leakiness.

There are several limitations to our study. A first limitation is the small patient population, therefore further studies with larger study populations are needed to confirm our findings. Secondly, because only one person was involved in the demarcation of the ROIs, we could not determine the intra- or interobserver agreement or reproducibility. Thirdly, in our study, rigid registration of the liver was used. Three lesions located in the left liver lobe showed an indefinable TIC, which suggests the strong influence of heart motions on these lesions. We think that registration of the lesions instead of the liver might provide better reduction of motion artefacts. Furthermore, we included only patients with HCA and FNH, which can overestimate sensitivity, specificity and diagnostic confidence. Finally, it is clear that the use of both IVIM and DCE-MRI lack standardization of imaging acquisition and analysis techniques. This might partially explain the wide variations in their values in literature.

In summary, this prospective preliminary study showed that IVIM parameter D and DCE-MRI parameter K^{trans} were useful in differentiating FNHs from HCAs in most cases, whereas ADC, V_e and TIC analyses were not.

REFERENCES

1. Le Bihan D, Breton E, Lallemand D, Grenier P, Cabanis E, Laval-Jeantet M. MR imaging of intravoxel incoherent motions: application to diffusion and perfusion in neurologic disorders. *Radiology* 1986; **161**: 401–7. doi: https://doi.org/10.1148/radiology.161.2.3763909
2. Luciani A, Vignaud A, Cavet M. Liver cirrhosis: intravoxel incoherent motion MR imaging—pilot study. *Radiology* 2008; **249**: 891–9. doi: https://doi.org/10.1148/radiol.2493080080
3. Le Bihan D. Intravoxel incoherent motion perfusion MR imaging: a wake-up call. *Radiology* 2008; **249**: 748–52. doi: https://doi.org/10.1148/radiol.2493081301
4. Koh DM, Collins DJ, Orton MR. Intravoxel incoherent motion in body diffusion-weighted MRI: reality and challenges. *AJR Am J Roentgenol* 2011; **196**: 1351–61. doi: https://doi.org/10.2214/ajr.10.5515
5. Qayyum A. Diffusion-weighted imaging in the abdomen and pelvis: concepts and applications. *Radiographics* 2009; **29**: 1797–810. doi: https://doi.org/10.1148/rg.296095521
6. d'Arcy JA, Collins DJ, Padhani AR, Walker-Samuel S, Suckling J, Leach MO. Informatics in radiology (infoRAD): magnetic resonance imaging workbench: analysis and visualization of dynamic contrast-enhanced MR imaging data. *Radiographics* 2006; **26**: 621–32.
7. Leach MO, Brindle KM, Evelhoch JL. The assessment of antiangiogenic and antivascular therapies in early-stage clinical trials using magnetic resonance imaging: issues and recommendations. *Br J Cancer* 2005; **92**: 1599–610. doi: https://doi.org/10.1038/sj.bjc.6602550
8. Tofts PS, Kermode AG. Measurement of the blood-brain barrier permeability and leakage space using dynamic MR imaging. Fundamental concepts. *Magn Reson Med* 1991; **17**: 357–67. doi: https://doi.org/10.1002/mrm.1910170208
9. Sourbron SP, Buckley DL. On the scope and interpretation of the Tofts models for DCE-MRI. *Magn Reson Med* 2011; **66**: 735–45. doi: https://doi.org/10.1002/mrm.22861
10. Katabathina VS, Menias CO, Shanbhogue AK, Jagirdar J, Paspulati RM, Prasad SR. Genetics and imaging of hepatocellular adenomas: 2011 update. *Radiographics* 2011; **31**: 1529–43. doi: https://doi.org/10.1148/rg.316115527
11. Hussain SM, Terkivatan T, Zondervan PE. Focal nodular hyperplasia: findings at state-of-the-art MR imaging, US, CT, and pathologic analysis. *Radiographics* 2004; **24**: 3–17. doi: https://doi.org/10.1148/rg.241035050
12. Coenegrachts K. Magnetic resonance imaging of the liver: new imaging strategies for evaluating focal liver lesions. *World J Radiol* 2009; **1**: 72–85.
13. Dyvorne H, Jajamovich G, Kakite S, Kuehn B, Taouli B. Intravoxel incoherent motion diffusion imaging of the liver: optimal *b*-value subsampling and impact on parameter precision and reproducibility. *Eur J Radiol* 2014; **83**: 2109–13. doi: https://doi.org/10.1016/j.ejrad.2014.09.003
14. Patel J, Sigmund EE, Rusinek H, Oei M, Babb JS, Taouli B. Diagnosis of cirrhosis with intravoxel incoherent motion diffusion MRI and dynamic contrast-enhanced MRI alone and in combination: preliminary experience.

J Magn Reson Imaging 2010; **31**: 589–600. doi: https://doi.org/10.1002/jmri.22081
15. Andreou A, Koh DM, Collins DJ. Measurement reproducibility of perfusion fraction and pseudodiffusion coefficient derived by intravoxel incoherent motion diffusion-weighted MR imaging in normal liver and metastases. *Eur Radiol* 2013; **23**: 428–34. doi: https://doi.org/10.1007/s00330-012-2604-1
16. Youden WJ. Index for rating diagnostic tests. *Cancer* 1950; **3**: 32–5. doi: https://doi.org/10.1002/1097-0142(1950)3:1<32::aid-cncr2820030106>3.0.co;2-3
17. Donati F, Boraschi P, Gigoni R, Salemi S, Falaschi F, Bartolozzi C. Focal nodular hyperplasia of the liver: diffusion and perfusion MRI characteristics. *Magn Reson Imaging* 2013; **31**: 10–16. doi: https://doi.org/10.1016/j.mri.2012.06.031
18. Grieser C, Steffen IG, Kramme IB. Gadoxetic acid enhanced MRI for differentiation of FNH and HCA: a single centre experience. *Eur Radiol* 2014; **24**: 1339–48. doi: https://doi.org/10.1007/s00330-014-3144-7
19. Grazioli L, Bondioni MP, Haradome H. Hepatocellular adenoma and focal nodular hyperplasia: value of gadoxetic acid-enhanced MR imaging in differential diagnosis. *Radiology* 2012; **262**: 520–9. doi: https://doi.org/10.1148/radiol.11101742
20. Bieze M, van den Esschert JW, Nio CY. Diagnostic accuracy of MRI in differentiating hepatocellular adenoma from focal nodular hyperplasia: prospective study of the additional value of gadoxetate disodium. *AJR Am J Roentgenol* 2012; **199**: 26–34. doi: https://doi.org/10.2214/ajr.11.7750
21. Huppertz A, Haraida S, Kraus A. Enhancement of focal liver lesions at gadoxetic acid enhanced MR imaging: correlation with histopathologic findings and spiral CT—initial observations. *Radiology* 2005; **234**: 468–78. doi: https://doi.org/10.1148/radiol.2342040278
22. Mohajer K, Frydrychowicz A. Characterization of hepatic adenoma and focal nodular hyperplasia with gadoxetic acid. *J Magn Reson Imaging* 2012; **36**: 686–96. doi: https://doi.org/10.1002/jmri.23701
23. Purysko AS, Remer EM, Coppa CP, Obuchowski NA, Schneider E, Veniero JC. Characteristics and distinguishing features of hepatocellular adenoma and focal nodular hyperplasia on gadoxetate disodium-enhanced MRI. *AJR Am J Roentgenol* 2012; **198**: 115–23. doi: https://doi.org/10.2214/ajr.11.6836
24. Agnello F, Ronot M, Valla DC, Sinkus R, Van Beers BE, Vilgrain V. High-*b*-value diffusion weighted MR imaging of benign hepatocellular lesions: quantitative and qualitative analysis. *Radiology* 2012; **262**: 511–19. doi: https://doi.org/10.1148/radiol.11110922
25. Doblas S, Wagner M, Leitao HS. Determination of malignancy and characterization of hepatic tumor type with diffusion-weighted magnetic resonance imaging: comparison of apparent diffusion coefficient and intravoxel incoherent motion-derived measurements. *Invest Radiol* 2013; **48**: 722–8. doi: https://doi.org/10.1097/rli.0b013e3182915912
26. Morelli JN, Michaely HJ, Meyer MM, Rustemeyer T, Schoenberg SO, Attenberger UI. Comparison of dynamic and liver-specific gadoxetic acid contrast-enhanced MRI *versus* apparent diffusion coefficients. *PLoS One* 2013; **8**: e61898.
27. Wang M, Li X, Zou J, Chen X, Chen S, Xiang W. Evaluation of hepatic tumors using intravoxel incoherent motion diffusion-weighted MRI. *Med Sci Monit* 2016; **22**: 702–9. doi: https://doi.org/10.12659/msm.895909
28. Yoon JH, Lee JM, Yu MH, Kiefer B, Han JK, Choi B. Evaluation of hepatic focal lesions using diffusion-weighted MR imaging: comparison of apparent diffusion coefficient and intravoxel incoherent motion-derived parameters. *J Magn Reson Imaging* 2014; **39**: 276–85. doi: https://doi.org/10.1002/jmri.24158
29. Zhu L, Cheng Q, Luo W, Bao L, Guo G. A comparative study of apparent diffusion coefficient and intravoxel incoherent motion-derived parameters for the characterization of common solid hepatic tumors. *Acta Radiol* 2015; **56**: 1411–18. doi: https://doi.org/10.1177/0284185114559426
30. Watanabe H, Kanematsu M, Goshima S. Characterizing focal hepatic lesions by free-breathing intravoxel incoherent motion MRI at 3.0 T. *Acta Radiol* 2014; **55**: 1166–73. doi: https://doi.org/10.1177/0284185113514966
31. Leporq B, Saint-Jalmes H, Rabrait C. Optimization of intra-voxel incoherent motion imaging at 3.0 Tesla for fast liver examination. *J Magn Reson Imaging* 2015; **41**: 1209–17. doi: https://doi.org/10.1002/jmri.24693
32. Grazioli L, Morana G, Kirchin MA, Schneider G. Accurate differentiation of focal nodular hyperplasia from hepatic adenoma at gadobenate dimeglumine-enhanced MR imaging: prospective study. *Radiology* 2005; **236**: 166–77. doi: https://doi.org/10.1148/radiol.2361040338